2009

# Measurements of Sea Surface Height Variability in the Eastern South Atlantic from Pressure Sensor–Equipped Inverted Echo Sounders: Baroclinic and Barotropic Components

Sheekela Baker-Yeboah
*University of Rhode Island*

D. Randolph Watts
*University of Rhode Island*, randywatts@uri.edu

Deirdre A. Byrne



## Citation/Publisher Attribution

Baker-Yeboah, S., D.R. Watts, and D.A. Byrne, 2009: Measurements of Sea Surface Height Variability in the Eastern South Atlantic from Pressure Sensor–Equipped Inverted Echo Sounders: Baroclinic and Barotropic Components. *J. Atmos. Oceanic Technol.,* **26**, 2593–2609, https://doi.org/10.1175/2009JTECHO659.1
Available at: https://doi.org/10.1175/2009JTECHO659.1

Measurements of Sea Surface Height Variability in the Eastern South Atlantic from Pressure Sensor–Equipped Inverted Echo Sounders: Baroclinic and Barotropic Components

# Measurements of Sea Surface Height Variability in the Eastern South Atlantic from Pressure Sensor–Equipped Inverted Echo Sounders: Baroclinic and Barotropic Components

SHEEKELA BAKER-YEBOAH* AND D. RANDOLPH WATTS

*Graduate School of Oceanography, University of Rhode Island, Narragansett, Rhode Island*

DEIRDRE A. BYRNE

*School of Marine Sciences, University of Maine, Orono, Maine*

(Manuscript received 23 July 2008, in final form 2 July 2009)

ABSTRACT

Variability in sea surface height (SSH) can be decomposed into two contributions: one from changes in mass in the water column (barotropic) and the other from purely steric changes (baroclinic). Both contributions can be determined from data recorded by a pressure sensor–equipped inverted echo sounder (PIES). PIES data from the Agulhas South Atlantic Thermohaline Experiment (ASTTEX) were used, collected in the Cape Basin off South Africa, along 1000 km of an eddy corridor where Agulhas eddies carry cores of warm, salty Indian Ocean waters into the South Atlantic. The paper presents in detail the method used to convert PIES measurements into barotropic, baroclinic, and total SSH, and discusses the error budget. The baroclinic contribution is geopotential height (reference 4500 dbar), which can be determined from the measured vertical acoustic travel time together with a lookup curve based on the regional hydrography. The main error source is scatter about this curve that depends on the extent to which water masses advecting along each geopotential streamline may derive from different ocean regions. The barotropic contribution can be determined from the bottom pressure measurements of the mass variation in the water column and has an uncertainty due to sensor calibration drift in two years corresponding to 1-cm water column height. The barotropic component accounts for 20% of the overall SSH variance and 47% during large signal intervals exceeding 15 cm. PIES data demonstrate via the two measurements that barotropic and baroclinic contributions may work independently or in concert in different mesoscale eddies. The combined structure need not be equivalent barotropic. In particular, deep barotropic eddies exhibit mesoscale spatiotemporal scales and may or may not be systematically tilted or aligned in space or time relative to baroclinic eddies.

## 1. Introduction

The main goals of this paper are 1) to show in detail how the baroclinic and barotropic contributions to sea surface height (SSH) can be measured by a pressure sensor–equipped inverted echo sounder (PIES) and 2) to quantify the uncertainties in these estimates. SSH varies because of changes in density and changes in total mass within the water column. The contribution from changes in the density profile is termed steric height, which can be calculated from the geopotential anomaly as a function of the temperature and salinity profiles relative to a deep reference pressure. The steric contribution is also commonly called the baroclinic contribution because variability in density profiles is often associated with sloping density surfaces across currents in the ocean. Additional contributions to steric height arise from processes with a relatively small slope in density surfaces across isobars, such as basin-scale warming and seasonal signals. These steric signals are broadly included under the expression ''baroclinic contribution to SSH.'' The mass-loading contribution can be calculated from the bottom pressure, which by hydrostatics is the integrated mass per square meter above the pressure sensor

* Current affiliation: Massachusetts Institute of Technology, Cambridge, Massachusetts.

*Corresponding author address:* Sheekela Baker-Yeboah, Department of Earth, Atmospheric and Planetary Sciences, MIT, 77 Massachusetts Avenue, MIT 54-1415, Cambridge, MA 02139.
E-mail: sbaker@mit.edu

DOI: 10.1175/2009JTECHO659.1

multiplied by the gravitational constant. We identify this mass loading as the barotropic contribution.

Our choice of terminology selects one of an infinite set of choices of depth at which to reference a baroclinic profile plus a depth-independent reference to produce the total profile. The literature contains various choices, each legitimate and suiting different purposes. We use a deep reference pressure (4500 dbar) for the baroclinic variations, which differs from dynamical modes, in which the baroclinic components are referenced middepth, have nonzero bottom velocity and bottom pressure, and carry zero transport. Under our terminology, the barotropic component accounts for all variations in mass loading, and the baroclinic (i.e., steric) component accounts solely for density changes at constant mass in the water column. This approach is consistent with Fofonoff (1962), who references baroclinic velocity profiles with a deep (near bottom) barotropic component. We present details of this method in section 2 and in the appendix.

There has been much interest in probing ocean dynamics by measuring SSH variability from satellite data. Its steric and nonsteric contributions are well recognized (Fukumori et al. 1998; Ponte 1999; Guinehut et al. 2006; Jayne et al. 2003). Just as hydrographic density profiles can measure the steric (baroclinic) component relative to an abyssal pressure level, the nonsteric mass-loading barotropic component can be measured with a bottom pressure sensor. As noted in the above citations, bottom pressure records are uncommon in the deep ocean, and the spatiotemporal scales of barotropic energy vary from region to region.

In some regions, measurements of SSH variability have been shown to contain substantial signals at periods shorter than 20 days, which Stammer et al. (2000) note would cause aliasing of altimeter measurements. In many regions this high-frequency signal is primarily barotropic (Tierney et al. 2000; Gille and Hughes 2001; Xu et al. 2008). Several studies have focused on the high-frequency barotropic response of the sea surface to pressure loading and wind stress at periods less than 20 days, and spatial scales greater than 1000 km (Luther et al. 1990; Chao and Fu 1995; Tierney et al. 2000; Stammer et al. 2000). Hourly samples of the barotropic and baroclinic SSH components are provided by PIES data, giving a well-resolved high-frequency signal. In the Agulhas leakage region, the focus of this study, the barotropic signal and the larger baroclinic signal contribute importantly to SSH at periods shorter than 20 days (Baker-Yeboah 2008; Byrne and McClean 2008).

Some of the largest rapid nontidal variations observed by altimeters have been due to meandering jets and mesoscale eddies (Fukumori et al. 1998), wherein the baroclinic contribution is strong. The deep ocean in the southeastern South Atlantic is particularly energetic at time scales associated with eddies, some of which have both baroclinic and barotropic structure (Clement and Gordon 1995; Van Aken et al. 2003). Understanding the structure of these eddies is important to improving our understanding of the meridional overturning circulation in the South Atlantic, as addressed in Gordon (1985) and Biastoch et al. (2008). In section 3, we present three examples from PIES data of mesoscale eddies in the Agulhas leakage region that contribute different magnitudes of barotropic and baroclinic SSH variability. We discuss sources of error in these data in section 4, followed by a separate discussion on scatter in the inverted echo sounder (IES) lookup curve in section 5. Scatter in the lookup curve is related to variability in water properties, not to instrument error. Section 6 presents the summary and conclusions.

## 2. Data and methods

This study is based on data from the Agulhas–South Atlantic Thermohaline Transport Experiment (ASTTEX). During ASTTEX, 12 PIES instruments were deployed along a *Jason-1* ground track, as indicated by the squares in Fig. 1. The ASTTEX array spanned the Agulhas ''eddy corridor'' (Garzoli and Gordon 1996), a route for interocean exchange. Eddies produce strong SSH signals in the PIES data, and examples are presented in this work of eddies having primarily baroclinic SSH, mixed baroclinic–barotropic SSH, and primarily barotropic SSH. In these case studies, AVISO satellite altimeter SSH records (AVISO 2006) are used in conjunction with PIES baroclinic and barotropic SSH components (section 3).

PIES instruments measure bottom pressure $p_{\rm bot}$ and round-trip acoustic travel time (Fig. 2). Acoustic travel time, which varies with the temperature and salinity through the water column, is used to estimate the baroclinic contribution to SSH. At low frequencies, the barotropic velocity is in geostrophic balance with the barotropic pressure field and provides the 4500-dbar reference for the baroclinic field, as discussed in the appendix.

We use the hydrostatic equation to characterize the two different measures of SSH variability provided from PIES data:

$$\int_{-H}^{\eta'} dz = -\int_{p_{\rm bot}}^{p_a} \frac{1}{\rho g}\, dp,$$

where $\eta = \overline{\eta} + \eta'$ is SSH, $p_a$ is the surface atmospheric pressure, and $p_{\rm bot}$ is seafloor bottom pressure. This relation gives a partition of SSH into a baroclinic component ($\eta_{\rm bc}$) and a barotropic component ($\eta'_{\rm bt}$),

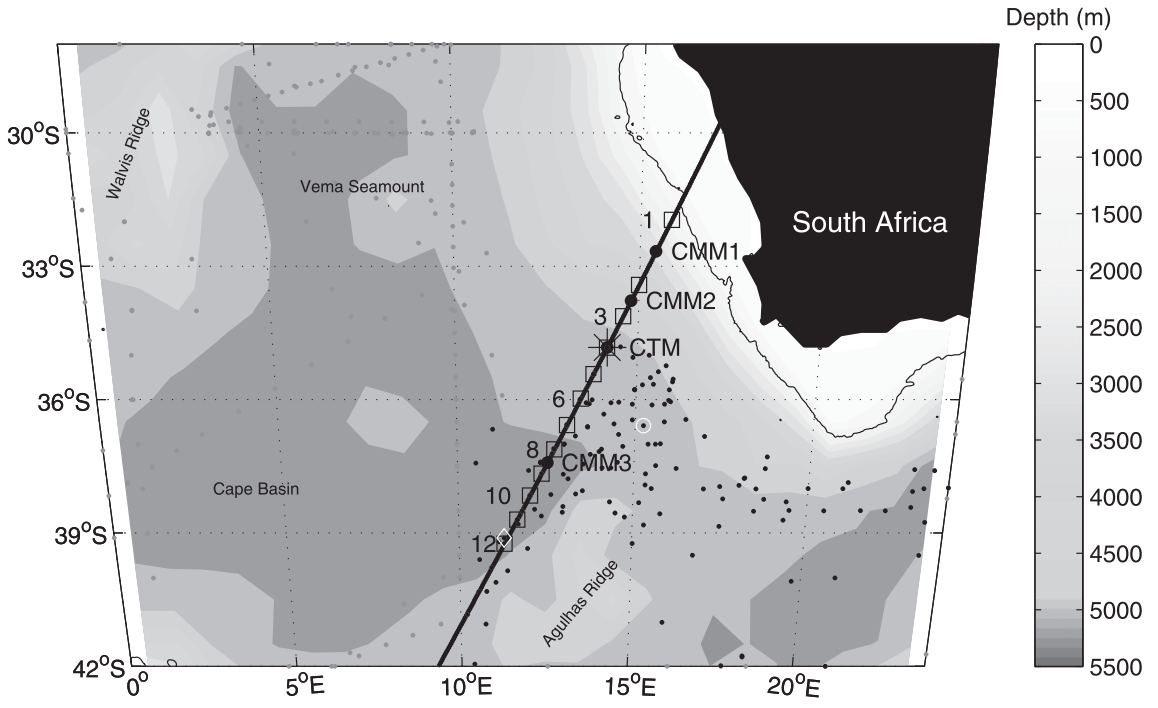


FIG. 1. The Agulhas South Atlantic Thermohaline Experiment (ASTTEX) array: 12 PIES (squares) and four CMMs (circles) along an altimeter ground track. Instruments are numbered from northeast to southwest. Dots represent locations of CTD data that are used in the $\tau$-to-$\phi$ technique (146 points in black). The data storage device did not function in PIES 5. Profiles of the circled dot and diamond-enclosed dot (near site 12) are discussed in section 5. The black contour line is at 500 m.

$$\eta_{\rm bc} = \frac{\phi_{\overline{P}}}{g} \quad \text{and}$$

$$\eta'_{\rm bt} = \frac{p_{\rm bot} - \overline{P}}{\rho_b g}$$

[see Eqs. (A9) and (A10)]. The IES data from the PIES measurements are converted to geopotential height (Fig. 9; appendix). This curve is called the IES lookup table and is based on the regional hydrographic data. These methods are based on Watts and Rossby (1977) and He et al. (1998). We can separate $\eta_{\rm bc}$ into $\overline{\eta_{\rm bc}}$ and $\eta'_{\rm bc}$, such that we can examine the time series $\eta_{\rm PIES} = \eta_{\rm bc} + \eta'_{\rm bt}$ or $\eta'_{\rm PIES} = \eta'_{\rm bc} + \eta'_{\rm bt}$, where $\eta'_{\rm bt}$ is based on measurements from the instrument's enclosed pressure sensor. For more details, see the appendix.

PIES measurements of $p_{\rm bot}$ were collected at 10-min intervals using the Paroscientific Digiquartz pressure sensor and averaged to hourly values. The absolute accuracy of these pressure measurements is specified by Paroscientific to be 100 ppm (Houston and Paros 1998) of the full-scale pressure—that is, 60 hPa (1 hPa $\approx$ 1 cm) for gauges capable of 6000 dbar. The sensor resolves $p_{\rm bot}$ to 0.1 hPa (IESUM 2006). The PIES instruments were tethered about 0.5 m off the seafloor. The tether is kept short so that the horizontal drag from near-bottom currents produces acceptably small mooring motion. For example, knowing the instrument buoyancy and estimating the drag from currents less than 25 cm s$^{-1}$, the mooring deflection angle from vertical can be estimated to be less than 5°. The resulting vertical deflection for a 50-cm tether is less than 0.2 cm. The pressure sensors were prestressed in the laboratory prior to deployment for about 2 months to reduce drift; however, a small drift of up to 10 hPa over a 27-month deployment period still occurred (Table 1). After data retrieval, the drift for each instrument was estimated by a linear fit to the 27-month $p_{\rm bot}$ time series and was removed. Next, the barotropic tide was removed using response analysis (Munk and Cartwright 1966). We chose to remove only semidiurnal and diurnal components. Long-period tides were not removed—fortnightly tides ~0.6 cm (Schwiderski 1982) and pole tides ~0.5 cm (Cartwright 2000). The time-mean pressure at each instrument location was removed, $p' = p_{\rm bot} - \overline{P}$, to give the residual pressure, which has an uncertainty of 1 hPa (Watts and Kontoyiannis 1990).

PIES measurements of round-trip acoustic travel time $\tau_{\rm ies}$ comprise 24 pings per hour (12 kHz, with a ping duration of 6 ms). The value $\tau_{\rm ies}$ is inversely proportional to the speed of sound $c$ integrated through the water column (path depicted as a dash–dot line in Fig. 2).

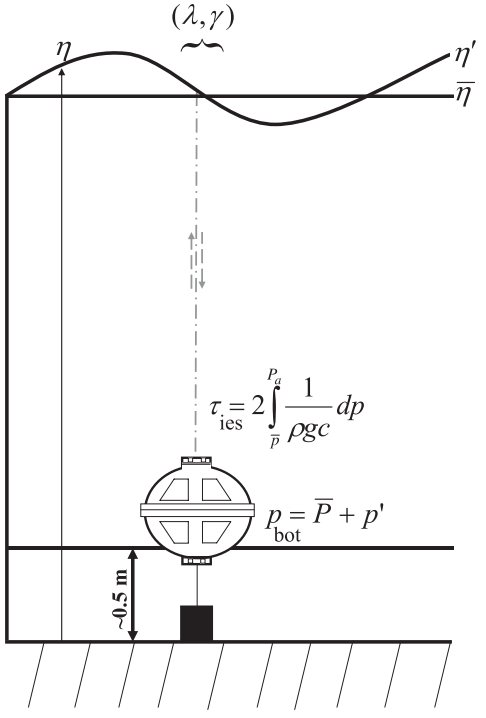


FIG. 2. A PIES instrument moored near the seafloor at latitude $\lambda$ and longitude $\gamma$. Measurements include bottom pressure ($p_{\text{bot}}$) and round-trip acoustic travel time ($\tau_{\text{ies}}$).

Instrument details can be found in Chaplin and Watts (1984) and IESUM (2006). Measurements of $\tau_{\text{ies}}$ are resolved to 0.05 ms, with insignificant drift. However, reflection off the wavy sea surface introduces scatter of about 2 ms in individual echoes. The hourly groups of 24-ping data were processed into single hourly values after windowing to remove erroneous data spikes and sorting to find the first quartile value. These values were low-pass filtered using a sixth-order Butterworth filter with a 29-h cutoff, run forward and backward. The processed hourly $\tau_{\text{ies}}$ values (Baker-Yeboah 2008) have an accuracy of about 0.4 ms, and the 29-h low-pass-filtered data have an accuracy of about 0.08 ms (Table 1).

## 3. PIES baroclinic and barotropic SSH variability

### *a. Baroclinic and barotropic SSH variability*

The time series of PIES total SSH variability $\eta'_{\text{PIES}}$ and the two components $\eta'_{\text{bc}}$ and $\eta'_{\text{bt}}$ are shown in Figs. 3a and 3b. Adjacent sites along the array exhibit large amplitude features, consistent from site to site (Figs. 3a and 3b). Although the $\eta'_{\text{PIES}}$ curve (black) usually follows the $\eta'_{\text{bc}}$ curve (red), the $\eta'_{\text{bt}}$ curve (gray) provides a separate and often important contribution to the total SSH curve. At all sites $\eta'_{\text{bt}}$ intermittently makes a substantial contribution to $\eta'_{\text{PIES}}$, as indicated by the shaded time intervals in Figs. 3a and 3b. The shaded regions will be addressed in section 3b.

TABLE 1. Error budget for PIES data. NA is not applicable.

| PIES error budget | Measurement uncertainty | Height uncertainty (cm) |
|---|---|---|
| Atmospheric pressure IB effect in $p_{\text{bot}}$ | NA | NA |
| Atmospheric pressure IB effect in $\tau_{\text{ies}}$ | 0.13 ms | 0.3 |
| Geophysical: sea state scatter | | |
| One ping | 2.00 ms | |
| 24 pings | 0.40 ms | |
| Low-pass filtered | 0.08 ms | 0.2 |
| Geophysical: sea state bias | +0.05 ms | 0.1 |
| Spline-curve lookup error (ASTTEX region) | 0.55 $m^2$ $s^{-2}$ | 5.5 ± 1 |
| Tides: ocean | | 0.1 |
| Instrumental: pressure sensor drift | 10 hPa | |
| Pressure drift residual | 1 hPa | 1.0 |
| Instrumental: mooring motion | | 0.2 |
| Total | | 5.6 ± 1 |

The record at site 1 differs from the other time series along the ASTTEX array, having relatively low SSH variability for both $\eta'_{\text{bc}}$ and $\eta'_{\text{bt}}$. Located on the continental slope where the bottom depth is ~1077 m, site 1 lacked the strong episodic low-frequency signals that typified other sites. Baker-Yeboah (2008) provides a further discussion on the spectra.

The root-mean-square (rms) fluctuations in $\eta'_{\text{PIES}}$, $\eta'_{\text{bc}}$, and $\eta'_{\text{bt}}$ for sites 1–12 are listed in Table 2, and the variances are plotted in Fig. 4. The rms variability for $\eta'_{\text{PIES}}$ was greater than or equal to 15 cm at sites 2–12 and peaked at 24 cm at site 7. The rms variability of $\eta'_{\text{bc}}$ was greater than or equal to 14 cm for sites 2–12 and peaked at 18 cm near sites 6 and 7, whereas the rms variability for $\eta'_{\text{bt}}$ was more than 5 cm at sites 3–12 and peaked at 11 cm at site 8.

The baroclinic and barotropic signals covaried, and the total variance is given by $\sigma^2 = \sigma^2_{\text{bc}} + \sigma^2_{\text{bt}} + 2\text{cov}$ (Fig. 4; Table 2). The ratios of variance for each component to the total variance were tabulated (Table 2) and reveal mean values of $\langle \sigma^2_{\text{bc}}/\sigma^2 \rangle = 0.71$, $\langle \sigma^2_{\text{bt}}/\sigma^2 \rangle = 0.16$, and $\langle 2\text{cov}/\sigma^2 \rangle = 0.13$. We estimated the confidence levels for the covariances based on the autocorrelation statistics of the time series (Emery and Thomson 2001). Covariances at the northernmost (site 1) and southernmost (sites 10–12) sites outside the eddy corridor did not differ significantly from zero. Covariances were significant at the 90% confidence level for sites 4–7 along the center of the eddy corridor.

*b. The importance of the barotropic component*

Although $\eta'_{bt}$ contributes only about 16% of the total variance averaged over the 11 sites, there are time intervals during which $\eta'_{bt}$ contributes 25%–100% of $\eta'_{PIES}$. We are interested in mesoscale variability and chose an SSH threshold value:

$$|\eta'_{PIES}| \geq 15 \text{ cm}. \quad (1)$$

We quantify the importance of the barotropic contribution by identifying those time intervals and events when the SSH anomaly reaches or exceeds the threshold of 15 cm and the ratio quantifying the importance of the barotropic contribution:

$${}^{\dagger}R_{bt} = \frac{|\eta'_{bt}|}{|\eta'_{bc}| + |\eta'_{bt}|} \geq 0.25. \quad (2)$$

The two criteria, ${}^{\dagger}R_{bt} \geq 0.25$ and $|\eta'_{PIES}| \geq 15$, isolate a subset of days ($^{\dagger}$) within the time series shown by the gray-shaded regions in Figs. 3a and 3b. The total number of days in the subset for each site is listed in Table 3 as ${}^{\dagger}B_1$.

Restricting our focus to the ${}^{\dagger}B_1$ days, the ratio ${}^{\dagger}\eta'_{bt}/{}^{\dagger}\eta'_{PIES}$ was calculated for each site. Mean and extrema of ${}^{\dagger}\eta'_{bt}/{}^{\dagger}\eta'_{PIES}$ are recorded in Table 3. The minimum and maximum values of ${}^{\dagger}\eta'_{bt}/{}^{\dagger}\eta'_{PIES}$ show that $\eta'_{bt}$ can even exceed $\eta'_{PIES}$, as indicated by values of ${}^{\dagger}\eta'_{bt}/{}^{\dagger}\eta'_{PIES} > 1$ and ${}^{\dagger}\eta'_{bt}/{}^{\dagger}\eta'_{PIES} < -1$. In such cases $\eta'_{bc}$ and $\eta'_{bt}$ have opposite signs and the resulting $\eta'_{PIES}$ can be smaller than the contributing parts. In Table 3, the column ${}^{\dagger}B_1$ reveals that within the eddy corridor at sites 3–10, the subset ($^{\dagger}$) comprises 16%–33% of the entire time series. We define the term $B_2$ as the number of days of large amplitude events where Eq. (1) applies. The ratio ${}^{\dagger}B_1/B_2$ quantifies the fraction of days with large amplitude events $|\eta'_{PIES}| > 15$ cm for which the barotropic signal contributes at least 25% to the total $\eta'_{PIES}$. Values of ${}^{\dagger}B_1/B_2$ convey that the nonsteric mass load contribution to $\eta'_{PIES}$ is substantial for 39%–59% of the time when $|\eta'_{PIES}|$ is large.

*c. Examples of mesoscale eddies in SSH variability*

We present three examples from the PIES time series data that illustrate the baroclinic, barotropic, and total SSH variability for mesoscale eddy events that transit the array. For comparison, we include results from AVISO *Jason-1* alongtrack data and plan-view AVISO maps of SSH variability. The time series for all sites were combined into time–space contour plots (Hovmöller-like diagrams) of baroclinic, barotropic, and total SSH variability (Figs. 5–7). Characteristic scales and propagation details of these and other events from PIES and satellite data are presented in Baker-Yeboah (2008).

Case 1 is from 1 December 2003–1 March 2004, during which a strong cyclonic event transits the array in the baroclinic and barotropic fields (Fig. 5). The cyclonic eddy is labeled C12 and C14 (the same eddy, encountering the array at different times) in the baroclinic field, L13 in the barotropic field, and C12C14 in the lower, plan-view, satellite panel. Both baroclinic and barotropic signals have similar amplitudes of about −25 cm, which combines to −50 cm of total SSH. Events in the baroclinic and barotropic fields are approximately in phase. Both span a period of about two months. At any instant in time, they span roughly 3°–4° of latitude ($\lambda$). There was no IES between sites 1 and 2, which is indicated by the gray hatched region between 32.3° and 33.1°S in the time–space plots of baroclinic and total SSH variability.

Case 2 is from 1 May 2004 to 1 July 2004, during which two, primarily baroclinic, strong anticyclonic events, labeled A13 and A14, transit the array (Fig. 6). They are flanked by mixed baroclinic–barotropic lows, in which the baroclinic field is not well represented by total SSH but is less intense. The barotropic event H16 transited the array along with A14. Together, they form a high in the middle of the box (June 2004 event) and reach about +45 cm in the baroclinic fields and slightly more than 5 cm in the barotropic field, which gives a total SSH of roughly +50 cm. The June 2004 event spanned a time period of about 1.5 months and at any instant in time spanned nearly 2° of latitude. The May 2004 event is out of phase, with a baroclinic high positioned over a barotropic low center (resulting in a combined SSH of less than +50 cm), whereas the June 2004 event is in phase in the baroclinic and barotropic fields. The May and June 2004 events are Agulhas rings, which are discussed further in Baker-Yeboah (2008).

Case 3 is from 1 January 2005 to 1 April 2005, when a strong barotropic anticyclonic event (H22) and a mixture of baroclinic anticyclonic and cyclonic events cross the array (Fig. 7). The baroclinic events have amplitudes of ±25 cm. The barotropic event reaches +30 cm. Unlike the previous cases, the amplitudes, sizes, and periods of the barotropic and baroclinic events differ. The total SSH suggests a single anticyclonic event (A22 and H22), lasting about one month and spanning roughly 3° of latitude, but it is actually the sum of separate constituent events. The other nearby baroclinic events last for less than half a month and span only about 1° of latitude. The barotropic event spans about one month and almost 2° of latitude. The SSH components from PIES clearly distinguish the separate baroclinic and barotropic features that come in contact with and/or cross the array during this time period.

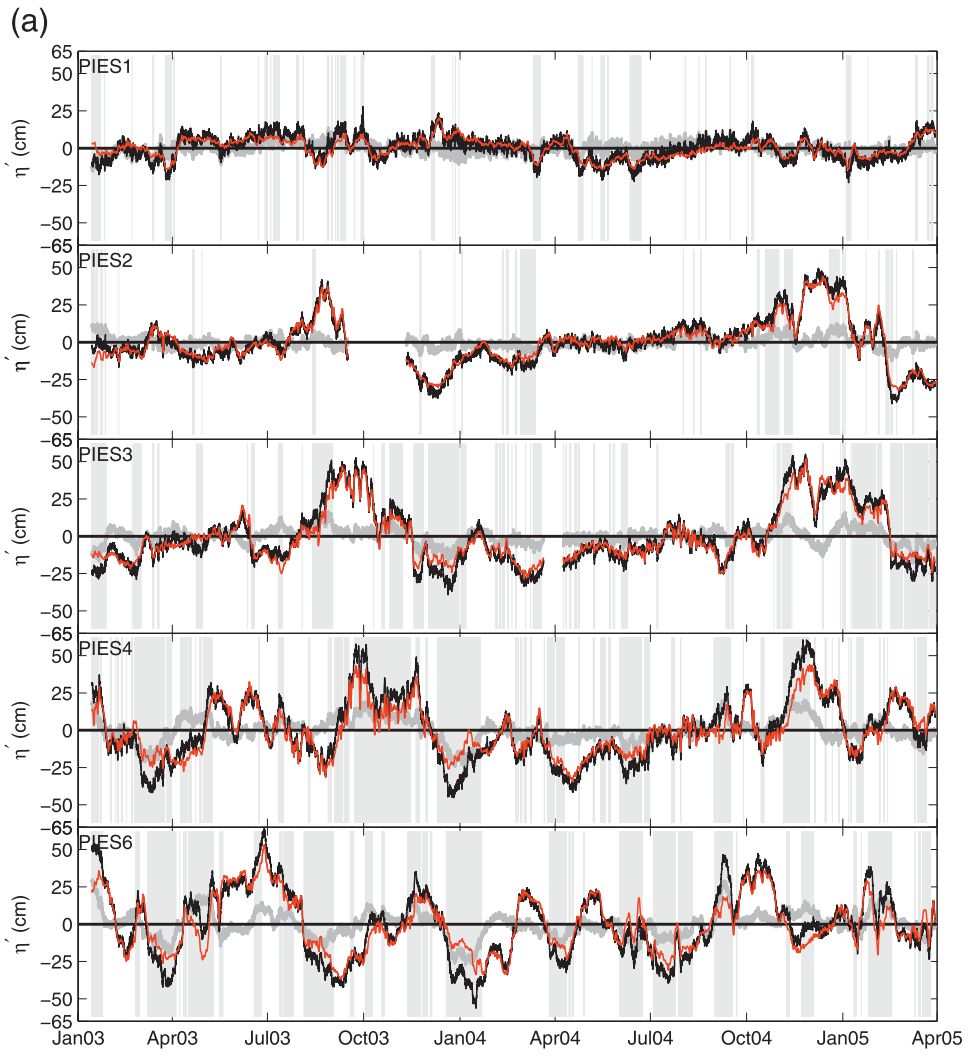


FIG. 3. (a) SSH variability from PIES sites: $\eta'_{bt}$ (gray), $\eta'_{bc}$ (red), and $\eta'_{PIES}$ (black). The red curve is often close to the black curve. The shaded regions highlight times during which $\eta'_{bt}$ can influence the total sea level variability, when $^{\dagger}R_{bt} \geq 0.25$ and $|\eta'_{PIES}| \geq 15$ cm. (b) As in (a), but for sites 7–12.

PIES and AVISO data show good agreement for all three case studies, as illustrated by the similarity between panels (c) and (d) in each of these three case studies (Figs. 5–7). The small differences between PIES and AVISO total SSH data are addressed in Baker-Yeboah (2008). We have restricted our attention to time periods when the SSH variability exceeds 15 cm to focus on mesoscale eddy variability, the topic of future studies (see the subsection below). We have illustrated in the current study that baroclinic and barotropic SSH variability can contribute equally to total SSH variability within some mesoscale eddies in the southeast South Atlantic, and that eddies in this region can have different vertical structures. Although PIES data provide a partitioning of SSH variability, these two measures of SSH can be combined to give total SSH variability as measured via satellite altimetry.

### d. *On the significance and dynamical implications of the observed structures*

The two measurements from PIES data capture barotropic and baroclinic contributions of mesoscale eddies that can move independently or in concert. The time series in Fig. 3 show barotropic and baroclinic highs and lows that coincide and those that do not. The strong highs are Agulhas rings or remnants of Agulhas rings (Baker-Yeboah 2008), and some of these events exhibit almost no barotropic signal. Agulhas rings near the formation region off of South Africa can have mixed barotropic–baroclinic velocity structure, as illustrated

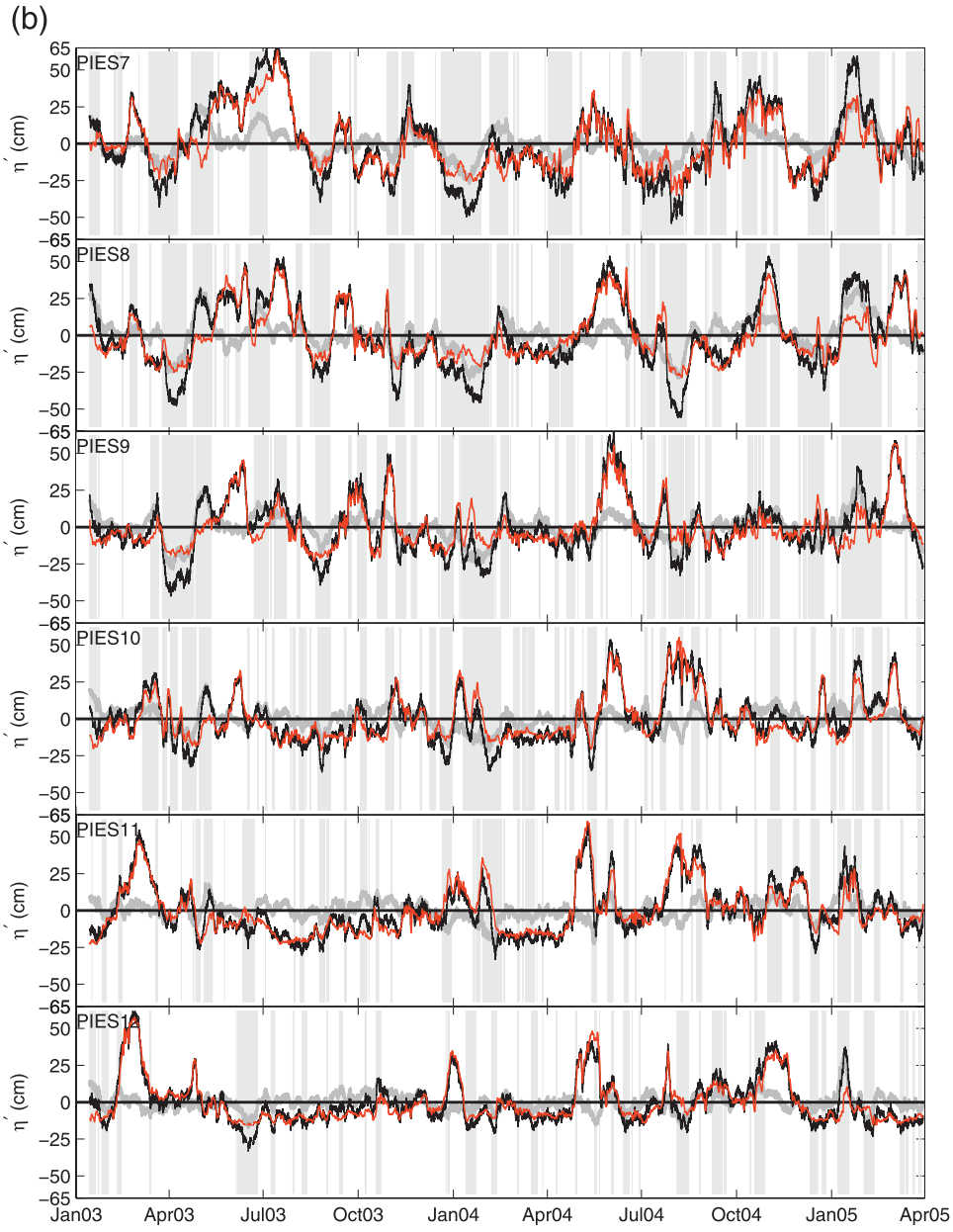


FIG. 3. (*Continued*)

in Van Aken et al. (2003), who report the deep extent of a ring's mixed baroclinic–barotropic velocity structure. That particular ring was younger, was located closer to the formation region, and had not crossed the Agulhas Ridge of seamounts; parts of the ridge system are shown in the lower panel of Fig. 5. It is possible that crossing the ridge alters the deep velocity signature of some Agulhas rings. Strong cyclonic eddies of mixed baroclinic and barotropic structure are also found in this region (e.g., the AVISO SSH maps in Figs. 5–7), and quantifying their structure and vertical tilt can help understand how they are generated. As illustrated in PIES baroclinic and barotropic fields (see the previous subsection), mesoscale eddy structures may be vertically aligned through the water column, laterally offset with a vertical tilt, or have different spatiotemporal evolution of their baroclinic and barotropic eddy structures as they translate. Thus, the combined structure of the eddies illustrated in the PIES data need not be equivalent barotropic.

The observed baroclinic and barotropic structures suggest that a range of eddy dynamics exist in the Cape Basin and lead to a number of dynamical issues for

TABLE 2. Variance results showing the significance of both barotropic and baroclinic signals. DOF refers to the number of degrees of freedom.

| PIES site | $\eta'_{\mathrm{PIES}}$ rms (cm) | $\eta'_{\mathrm{bc}}$ rms (cm) | $\eta'_{\mathrm{bt}}$ rms (cm) | $\frac{\sigma^2_{\mathrm{bt}}}{\sigma^2}$ | $\frac{\sigma^2_{\mathrm{bc}}}{\sigma^2}$ | $\frac{2\mathrm{cov}}{\sigma^2}$ | $\mathrm{DOF}_{\mathrm{bt}}$ | $\mathrm{DOF}_{\mathrm{bc}}$ |
|---|---|---|---|---|---|---|---|---|
| 1 | 8 | 6 | 4 | 0.25 | 0.60 | 0.15 | 26 | 20 |
| 2 | 16 | 14 | 4 | 0.05 | 0.82 | 0.12 | 36 | 14 |
| 3 | 20 | 17 | 5 | 0.07 | 0.75 | 0.18 | 36 | 14 |
| 4 | 21 | 16 | 8 | 0.14 | 0.61 | 0.25 | 26 | 24 |
| 6 | 23 | 18 | 9 | 0.15 | 0.64 | 0.21 | 35 | 24 |
| 7 | 24 | 18 | 10 | 0.16 | 0.57 | 0.28 | 34 | 23 |
| 8 | 23 | 17 | 11 | 0.22 | 0.58 | 0.20 | 37 | 27 |
| 9 | 19 | 15 | 9 | 0.24 | 0.60 | 0.16 | 40 | 45 |
| 10 | 16 | 15 | 7 | 0.18 | 0.80 | 0.02 | 38 | 36 |
| 11 | 17 | 16 | 6 | 0.14 | 0.94 | −0.08 | 41 | 28 |
| 12 | 15 | 14 | 6 | 0.13 | 0.88 | −0.01 | 65 | 31 |

further study. Note that the spatial scales for barotropic motions are small compared to the barotropic Rossby radius of deformation (~2000 km). The mixed baroclinic and barotropic structure of these cyclonic and anticyclonic eddies and how they compare to other observations of Agulhas eddies are discussed in more detail in Baker-Yeboah (2008). That work demonstrates the good agreement between altimeter and PIES SSH estimates [as suggested by comparing panels (c) and (d) in Figs. 5–7], uses the altimeter SSH data to map and track the eddies that transit the ASTTEX array, and addresses nonlinear eddy–eddy interactions of vertically and laterally coupled behavior and eddy interaction with topography. Based on observations presented herein, a number of numerical simulations and process studies are underway.

## 4. Sources of error in PIES SSH variability

Table 1 summarizes the sources of error in the PIES data. Equations (A17) and (A18) clarify that the PIES bottom pressures are not affected by the inverted barometer (IB) effect $\eta_{\mathrm{IB}}$, and hence contain no uncertainty due to $\eta_{\mathrm{IB}}$ contamination. However, in this work we have neglected a small contribution in the IES measurements of $\tau$ due to $\eta_{\mathrm{IB}}$:

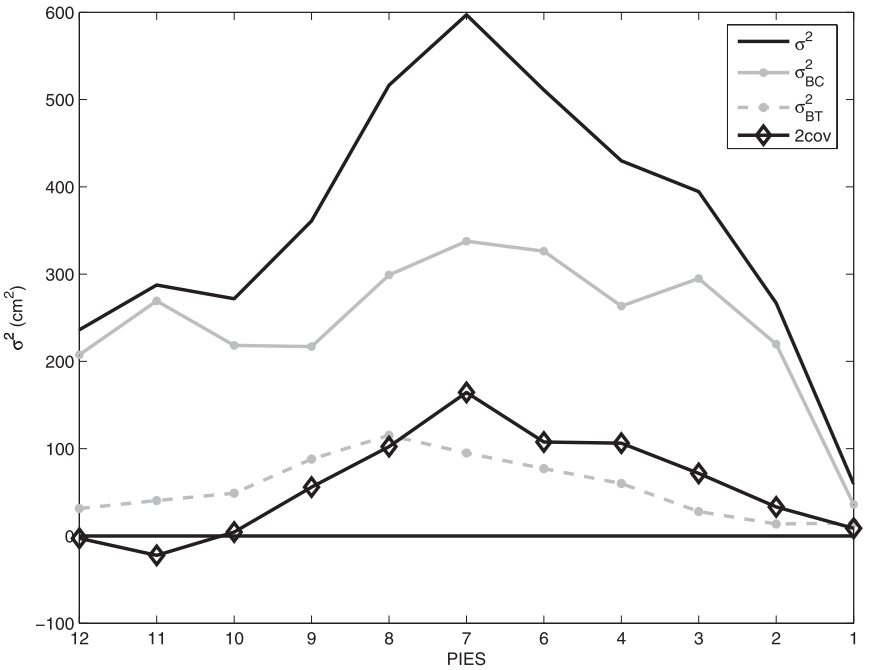


FIG. 4. SSH variance curves: total variance (black curve), baroclinic (solid gray curve), and barotropic (dashed gray curve), and covariance plotted as 2cov (solid line with diamonds).

TABLE 3. Results showing the importance of the barotropic component: ${}^{\dagger}B_1$ is the number of days when ${}^{\dagger}R_{\rm bt} \geq 0.25$ and $|\eta'_{\rm PIES}| \geq 15$ cm. Here $B_2$ is the number of days of large-amplitude events where $|\eta'_{\rm PIES}| \geq 15$ cm. The ratio ${}^{\dagger}B_1/B_2$ quantifies the fraction of large-amplitude events for which the barotropic signal contributes more than 25%.

| PIES site | $\frac{{}^{\dagger}\eta'_{\rm bt}}{{}^{\dagger}\eta'_{\rm PIES}}$ min | $\frac{{}^{\dagger}\eta'_{\rm bt}}{{}^{\dagger}\eta'_{\rm PIES}}$ max | $\frac{{}^{\dagger}\eta'_{\rm bt}}{{}^{\dagger}\eta'_{\rm PIES}}$ mean | ${}^{\dagger}B_1$ (days) (of 806 days) | $\frac{{}^{\dagger}B_1}{B_2}$ |
|---|---|---|---|---|---|
| 1 | 0.25 | 0.79 | 0.43 | 25 | 0.64 |
| 2 | −0.54 | 0.60 | 0.35 | 31 | 0.16 |
| 3 | −0.65 | 0.78 | 0.36 | 135 | 0.39 |
| 4 | −0.69 | 1.33 | 0.43 | 198 | 0.50 |
| 6 | −0.69 | 1.27 | 0.46 | 205 | 0.46 |
| 7 | −0.68 | 1.74 | 0.47 | 268 | 0.58 |
| 8 | −0.88 | 1.43 | 0.53 | 245 | 0.57 |
| 9 | −0.69 | 1.73 | 0.58 | 179 | 0.59 |
| 10 | −0.89 | 1.16 | 0.45 | 126 | 0.51 |
| 11 | −1.37 | 1.37 | 0.41 | 80 | 0.27 |
| 12 | −0.58 | 1.45 | 0.45 | 81 | 0.44 |

$$\tau_{\rm IB} = 2\frac{p_a - \overline{P}_a}{\rho_s g c_s}, \tag{3}$$

because we do not have accurate measurements of $p_a - \overline{P}_a$. The surface layer sound speed is given by $c_s$. Equation (3) gives $d\tau_{\rm IB}/dp_a \approx 0.013$ ms hPa$^{-1}$. For fluctuations in $p_a$ of about 10-hPa rms, we get $\tau_{\rm IB} \sim 0.13$ ms. Based on the distribution of water properties (see Fig. 8 and section 5), the slope of the lookup curve $\Delta\phi/\Delta\tau$ (Fig. 9) in centimeters per millisecond is approximately 2.5 cm ms$^{-1}$. Therefore, we estimate that this contributes an rms error of 0.3 cm to $\eta'_{\rm bc}$ (Table 1). In principle the National Centers for Environmental Prediction (NCEP) atmospheric pressure fields could be used to make this correction. However, because measurements of $p_a$ are sparse in the South Atlantic Ocean, applying the NCEP pressure fields might simply increase the total uncertainty of our measurements and thus they were not used.

Surface waves cause scatter in the IES measurements ($\tau$) with a standard deviation of ~2 ms (within hourly groupings). Elevated significant wave height (SWH) is known to increase scatter in $\tau$, but the detector design avoids early or late bias, by two effects that tend to cancel. The acoustic reflections off wave troughs tend to shorten $\tau$. For example, an 8-m SWH would shorten $\tau$ by about −0.25 ms. This is offset in the PIES echo detector and processing by higher ambient noise that lengthens the detection of travel time. The two effects counter each other and result in a net bias less than +0.05 ms (Table 1), which is small enough that we have not determined a correlation to SWH. The 24 measurements of $\tau$ per hour were quartile sampled into hourly values, which reduces the error to $2/\sqrt{24} = 0.4$ ms.

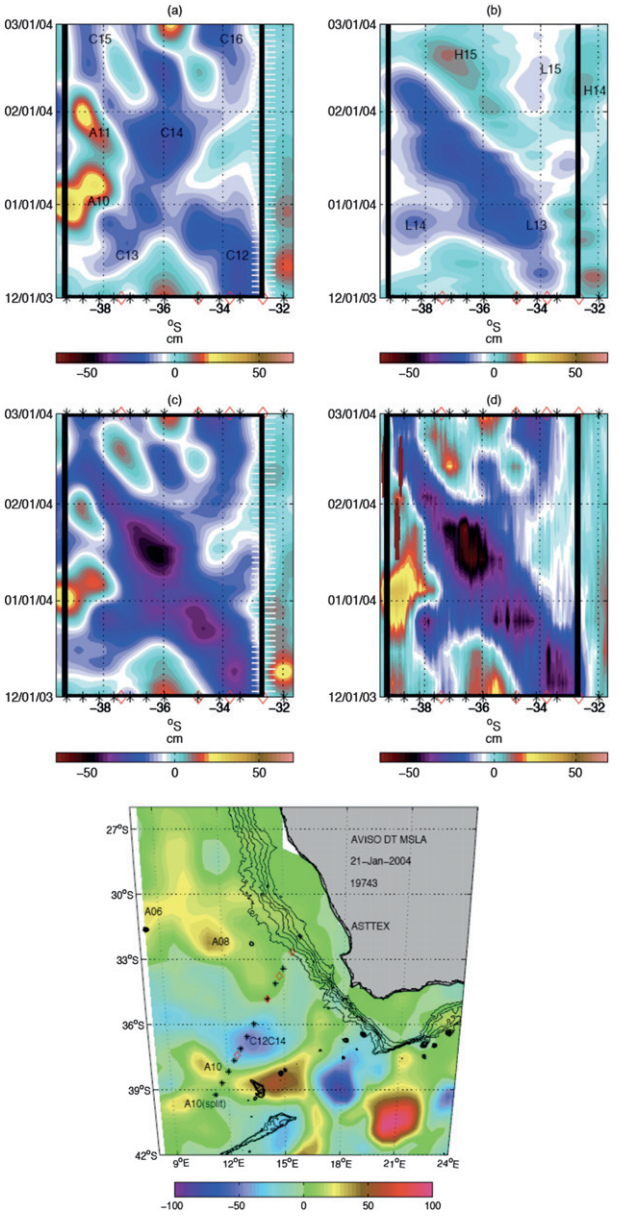


FIG. 5. Time–space plot of the 3-day low-pass-filtered (a) baroclinic and (b) barotropic components of SSH variability along the ASTTEX line for 1 Dec 2003–1 Mar 2004. (c) Total SSH variability [(a) + (b)] from 3-day low-pass-filtered PIES data. (d) SSH variability from *Jason-1* alongtrack AVISO up-to-date data. Hatched region along 32.3°–33.1°S indicates no IES data in field; (bottom) AVISO SSH anomaly (cm) map.

This error is reduced further with a 29-h low-pass filter to $0.4/\sqrt{29} = 0.08$ ms—which is equivalent to 0.2-cm error in $\eta_{\rm bc}$ using the functional spline-curve fit between $\phi_{4500}$ and $\tau$ (Fig. 9).

Two instrumental errors are associated with the PIES pressure measurements: drift in the pressure sensor calibration and vertical mooring motion. After prestressing

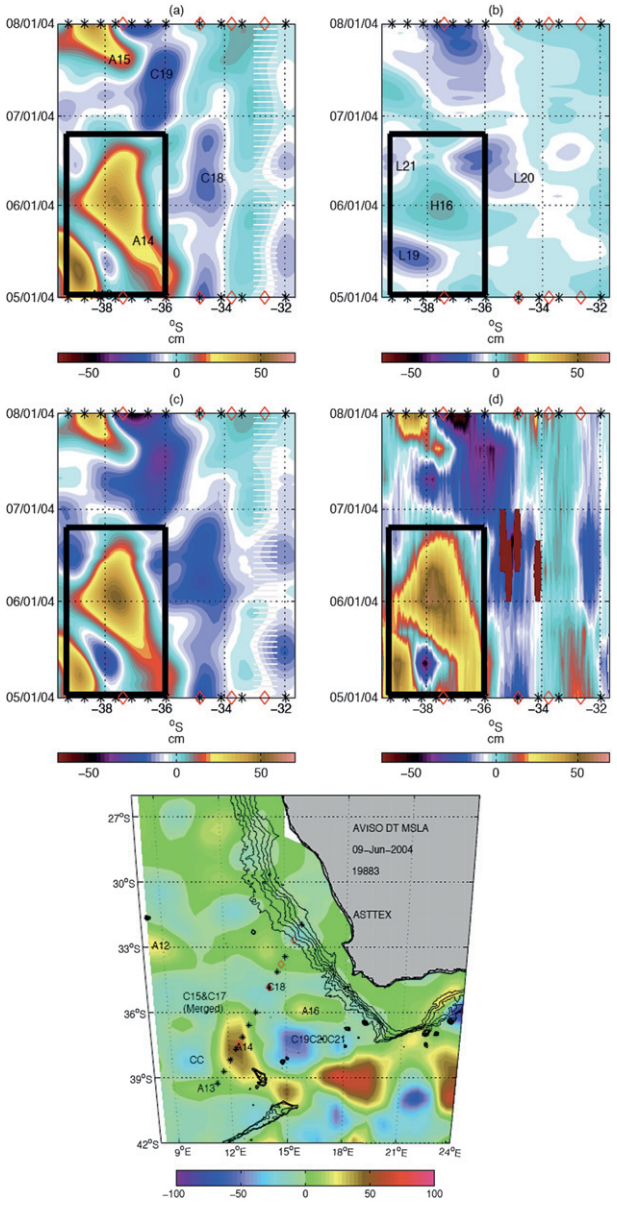


FIG. 6. Same as in Fig. 5, but for 1 May–1 Jul 2004.

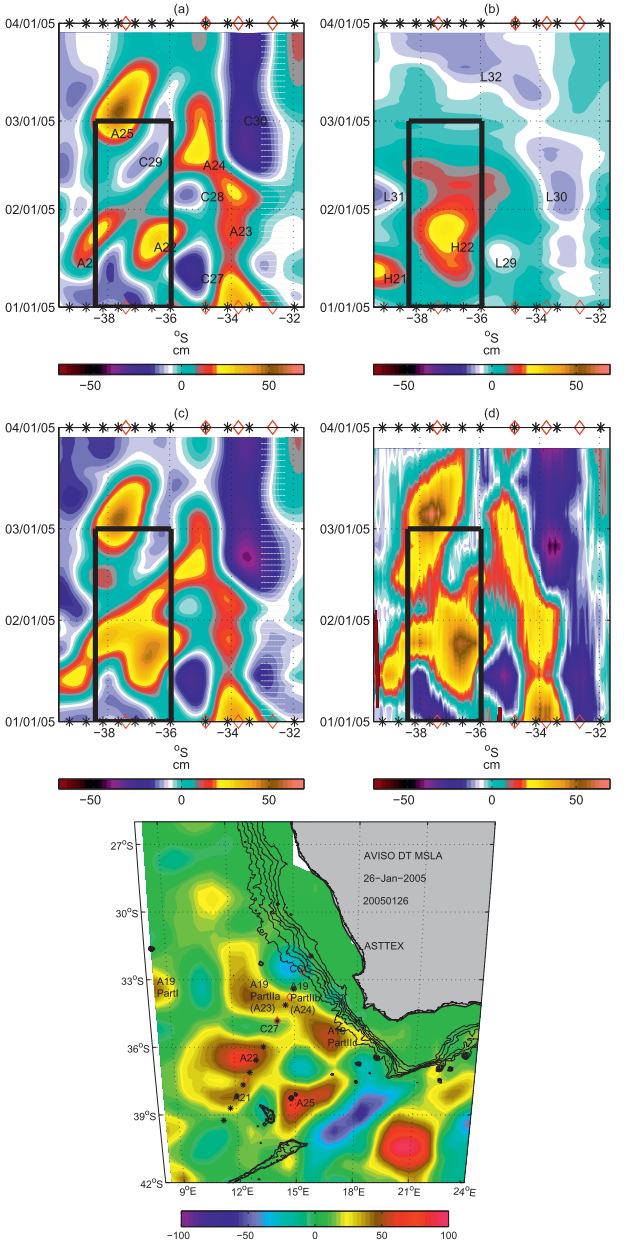


FIG. 7. Same as in Fig. 5, but for 1 Jan–1 Apr 2005.

the pressure sensors for two months or longer prior to the deployment, the pressure drift is typically ~10 hPa. After fitting and removing a linear trend, we estimate the residual drift error, which was ~1 hPa (1 cm), similar to that of Watts and Kontoyiannis (1990). The ASTTEX PIES instruments did not require anchor stands, because the bottom currents were almost always less than 30 cm $s^{-1}$. The tether length was 0.5 m, and the mooring vertical displacement was less than 0.2 cm.

The largest error in $\eta'_{\mathrm{PIES}}$ derives from the conversion of $\tau$ to dynamic height $\phi$. Although measurements of vertical acoustic travel time are generically labeled $\tau$, after calibrating these measurements using Eqs. (A12) and (A14), we use the more specific label of $\tau^*_{4500}$ (calibrated values). The lookup curve shown in Fig. 9 allows us to estimate $\phi$ relative to 4500 dbar from $\tau^*_{4500}$. To find $\phi$ without extrapolation, the assembled historical CTD data must represent the full range of observed calibrated $\tau^*_{4500}$ values (Baker-Yeboah 2008) from the PIES data, which is the case in this study. The standard error estimate for $\phi_{4500}$ is 0.55 $m^2$ $s^{-2}$, which is a 5.6-cm error for $\eta_{\mathrm{bc}}$ relative to 4500 dbar. The overall 5.6-cm rms uncertainty in $\eta_{\mathrm{bc}}$ is small compared

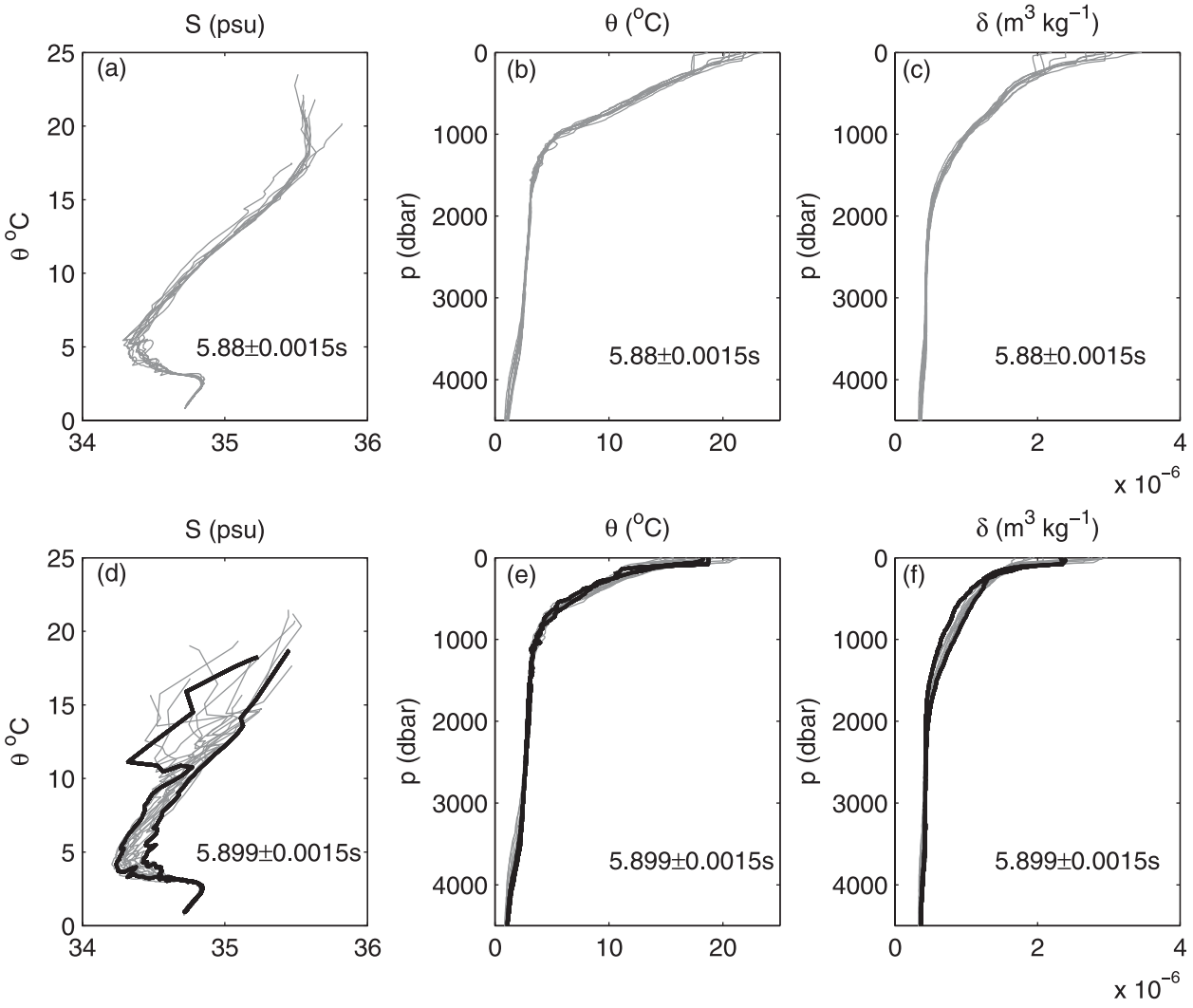


FIG. 8. Water properties contrasted for two $\tau$ groups: (a)–(c) $\tau = 5.880 \pm 0.0015$ s and (d)–(f) $\tau = 5.899 \pm 0.0015$ s. Potential temperature vs salinity is shown in (a) and (d); (b),(e) potential temperature profiles; and (c),(f) specific volume anomaly profiles. Thick black lines correspond to the fresher (diamond) and saltier (circle) outliers in Fig. 9.

to the 80-cm dynamic range observed in the Agulhas leakage region. The origin of this error, due to scatter about the $\tau$-to-$\phi$ lookup curve, is discussed in the following section.

## 5. Scatter in the lookup curve

The scatter about the $\tau$-to-$\phi$ lookup curve arises when profiles of temperature (potential temperature $\theta$) and salinity ($S$) contribute slightly differently to inverse sound speed (and its vertical integral $\tau$) than they do to specific volume anomaly $\delta$ (and its vertical integral $\phi$). In the Cape Basin, the scatter is specific to the circulation patterns and associated water masses within the region. Sun and Watts (2001) noted that the uncertainty is particularly large in this region because variations in salinity are large and affect density.

To understand how water mass variations are related to the $\tau$-to-$\phi$ lookup curve in Fig. 9, we divided the $\tau$ range into a ''warm section,'' where a higher mean water column temperature yields smaller $\tau$ values and a ''cold section,'' where a lower mean water column temperature yields larger $\tau$ values. A relatively tight $\tau$–$\phi$ relationship exists in the warm section (at low $\tau$), with 4.5 cm rms uncertainty for $\tau^*_{4500} < 5.886$ s. In contrast, the rms uncertainty is 6.5 cm for the cold section: $\tau^*_{4500} > 5.886$ s (large $\tau$).

In relation to Fig. 9, Fig. 8 presents examples of water properties within a narrow $\tau$ window of 3 ms within the warm section (Figs. 8a–8c) and the cold section

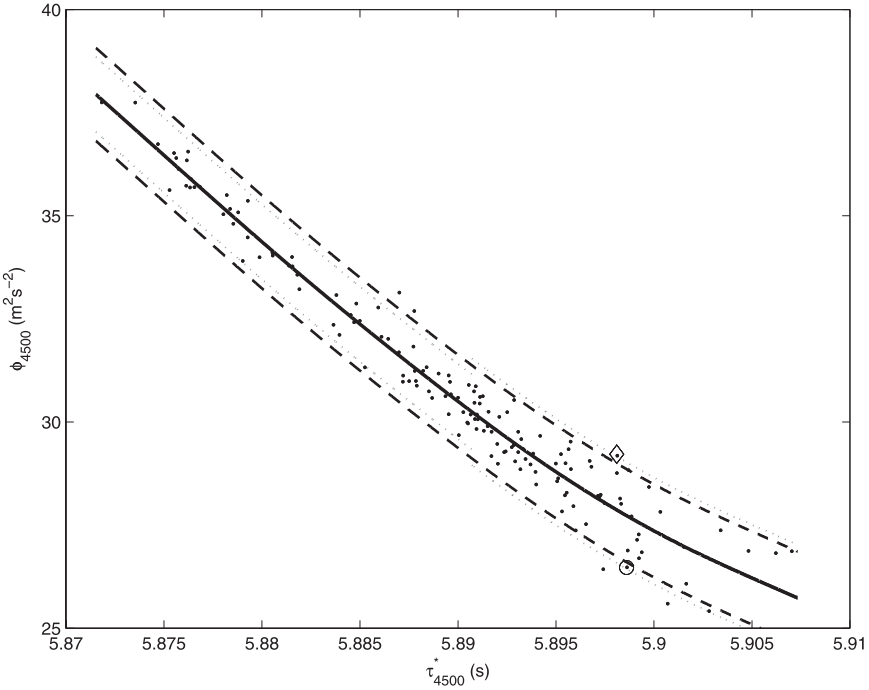


FIG. 9. The $\tau$-to-$\phi$ spline-curve fit used to determine steric height $\eta_{bc} = \phi_{4500}/g$ from geopotential anomaly $\phi$. Each dot represents $\tau^*_{4500}$ and $\phi_{4500}$ as computed from each CTD profile. The thick dashed curves are $\pm 2\sigma = 1.1$ m$^2$ s$^{-2}$. Light-gray dotted curves represent $\pm 2\sigma = 0.9$ m$^2$ s$^{-2}$ for the high $\phi$, low $\tau$, warm portion of the curve; and $\pm 2\sigma = 1.3$ m$^2$ s$^{-2}$ for the low $\phi$, high $\tau$, cold portion of the curve. The circled dot has a more saline profile compared to the diamond-enclosed dot (fresher waters), although both have similar $\tau$ values.

(Figs. 8d–8f). Along the warm section, the $\theta$–$S$ relationship is relatively uniform from station to station (Fig. 8a), as are the $\theta$ profiles (Fig. 8b) and $\delta$ profiles (Fig. 8c). The thermocline is deep, with a weak thermostad near 10°C, uniquely identified as originating in the Indian Ocean thermocline (Olson et al. 1992). This range of $\tau$ and $\phi$ values exists in the southwestern Indian Ocean and the Agulhas Retroflection, excluding stations north of the ASTTEX array. Recall that the location of the ASTTEX array was chosen to observe Agulhas rings shortly after they pinch off from the Agulhas Retroflection loop current. Consequently, we find that features with low $\tau$ values (warm portion) originate from the Agulhas Retroflection and that along the ASTTEX line these values indicate the presence of recently formed Agulhas rings, which carry cores of warm salty water. The low scatter of those profiles arises because $\theta$ and $S$ properties have not yet interleaved with surrounding colder waters.

In contrast, the cold section of Fig. 9 exhibits greater variety because of the presence of $\theta$ and $S$ profiles that have similar $\tau$ but different $\phi$ values. In Fig. 8e, $\theta$ profiles are again narrowly distributed around a central profile with relatively shallow thermocline. However, salinity shows greater variability (cf. Figs. 8d and 8a). In particular, notice the two outliers in the cold section in Fig. 9: one of high $\phi$ (diamond) and one of low $\phi$ (circle). These two stations are displayed as bold lines in Fig. 8 (bottom panels). The $\delta$ profiles clearly illustrate that dynamic height (area integral of $\delta$) differs for the two outliers, even though their $\tau$ values are nearly the same. Profiles with large $\tau$ values are commonly found both to the west in the Cape Basin along the South Atlantic subtropical front and to the east along the cool edge of the Agulhas in the Indian Ocean. The saltier profile in Fig. 8 (see also the station circled in Figs. 1 and 9) is of Agulhas origin, and the fresher profile is from the subtropical front (see also the diamond in Fig. 1 near PIES 12 and in Fig. 9). Both regions serve as sources for water along the ASTTEX line in the Cape Basin, and the presence of these different water types increases the scatter in the $\tau$–$\phi$ relationship.

Some profiles in the cold section (large $\tau$ side) interleave waters from two different oceans at different depths—for example, low-salinity Antarctic Intermediate Water (AAIW) of Atlantic origin under or overlying high-salinity thermocline waters of Indian origin. If the thermocline layer is thicker than the AAIW layer (or vice versa), then the $\delta$ profile and its $\phi$ will be most

influenced by the salinity values found in that respective layer. The observed outliers on the $\tau$–$\phi$ plot are from profiles that differ on large vertical scales, whereas small-scale interleaving would produce a relatively small effect on vertical-integral quantities. Nonlinear eddies can play an important role in such a water column process, and merit further study.

The vertical integral of inverse sound speed is affected differently from the vertical integral of specific volume anomaly (Fig. 8f). Note that a cold eddy with a salty core could have a $\phi$ that is about $2\sigma$ ($2 \times 6.5 = 13$ cm) above the $\tau$–$\phi$ curve, which would give an SSH 13 cm lower than estimated by $\eta_{\text{PIES}}$. Similarly, a cold eddy with a fresh core could have a $\phi$ that is about $2\sigma$ below the central $\tau$–$\phi$ curve, which would give an SSH 13 cm higher than estimated by $\eta_{\text{PIES}}$. Differences in water masses produce variability orthogonal to the $\tau$–$\phi$ curve and add to the uncertainty in the PIES estimates of SSH. Thus, using a central $\tau$–$\phi$ curve in this region where salinity profiles differ as illustrated can result in over- or underestimates by PIES SSH.

Byrne (2000) and Byrne et al. (2006) use in situ measurements of $\tau$ from PIES and satellite altimeter measurements of $\eta$ in the Cape Basin to take advantage of both the correlated and uncorrelated (orthogonal) information they provide, to estimate the temperature and salinity properties independent of one another. Their work is used for water property analysis. In the present paper, we examine the correlated information only—for analysis of SSH.

## 6. Summary and conclusions

PIES measurements provide a partitioning of SSH variability into baroclinic and barotropic SSH. The ASTTEX PIES measurements were used to quantify these components in the eastern South Atlantic Ocean, providing dynamical information on ocean variability at hourly temporal resolution. The largest error in the PIES-derived SSH is found to be from the lookup curve used to convert the inverted echo sounder measurements of acoustic travel time ($\tau$) to dynamic height ($\phi$): 4.5 cm for the warm section and 6.5 cm for the cold section of the curve. Scatter in the $\tau$-to-$\phi$ lookup curve arises when temperature and salinity contribute differently to travel time than to density. These different contributions are particularly strong in the Agulhas leakage region of the eastern South Atlantic, where different water masses from the Indian Ocean, South Atlantic Ocean, and Antarctic Circumpolar region converge.

Unlike other regions, such as the Kuroshio region, where $p_{\text{bot}}$ is thought to be relatively small (Teague et al. 1995), the barotropic component in the Cape Basin plays a substantial role in the total SSH variability. Although the baroclinic signal dominates the variance in total SSH variability over the 27-month period of data collection, during approximately half the time when the SSH is large ($>|15|$ cm), the barotropic contribution is more than 25% of SSH variability. There are even periods when the baroclinic contribution is negligible, such that the SSH variability is primarily barotropic. The barotropic component adds a comparable and independently varying SSH signal and should not be neglected in this region when interpreting altimeter data. The three case studies illustrated three diverse examples observed during this study: one eddy with barotropic and baroclinic eddy signals nearly aligned in the vertical, and one case with primarily baroclinic signal, and one case with comparably strong but primarily barotropic signal.

*Acknowledgments.* We thank the National Science Foundation for Grants OCE-0095572 and OCE-0099177 for the principal support of the ASTTEX project, and for Grant OCE-0221008. We also thank the National Aeronautics and Space Administration (NASA) for additional research support. We gratefully acknowledge the efforts of Karen Tracey and Mark Wimbush for writing and making available algorithms to process and detide the raw PIES data. We thank Gerry F. Chaplin for calibrating the PIES instruments and upgrading the firmware. We also acknowledge Kathy Donohue, Mark Wimbush, Jae-Hun Park, Tom Rossby, Peter Cornillon, and Glenn R. Flierl for their helpful comments and editorial suggestions. Furthermore, we thank the captain and crew of each ship (the R/V *Melville* and of the RRS *Discovery*) for helping us achieve the science goals of the deployment and recovery cruises, respectively. We appreciate the collaborative efforts of Marine and Coastal Management, South Africa, and the Ministry of Fisheries and Marine Resources, Namibia.

## APPENDIX

### Method of Determining Total SSH from PIES Data

#### *a. Barotropic and baroclinic SSH*

This section discusses how PIES measurements are used to determine SSH. The PIES data provide the two dynamical components of SSH: a barotropic contribution due to variable mass loading and a baroclinic or steric contribution due to variable density.

The PIES measurements are a function of latitude $\lambda$, longitude $\gamma$, and time $t$. We represent SSH as $\eta$, PIES bottom pressure as $p_{\text{bot}}$, and PIES hourly acoustic travel time as $\tau_{\text{hourly}}$:

$$\eta(\lambda, \gamma, t) = \overline{\eta}(\lambda, \gamma) + \eta'(\lambda, \gamma, t), \tag{A1}$$

$$p_{\text{bot}}(\lambda, \gamma, t) = \overline{P}(\lambda, \gamma) + p'(\lambda, \gamma, t), \quad \text{and} \tag{A2}$$

$$\tau_{\text{hourly}}(\lambda, \gamma, t) = \overline{\tau}_{\text{hourly}}(\lambda, \gamma) + \tau'_{\text{hourly}}(\lambda, \gamma, t), \tag{A3}$$

where we have separated these quantities into a time mean with respect to the common deployment period of the array of instruments (a 27-month period), indicated by an overbar ($^-$), and the time varying part, denoted by prime ($'$).

Integrating the hydrostatic relation, we have

$$\int_{-H}^{\eta'} dz = -\int_{p_{\text{bot}}}^{p_a} \frac{1}{\rho g}\, dp,$$

$$\eta' + H = \int_{\overline{P}_a}^{p_{\text{bot}}} \frac{1}{\rho g}\, dp + \int_{p_a}^{\overline{P}_a} \frac{1}{\rho g}\, dp, \quad \text{and}$$

$$\eta' + H = \int_{\overline{P}_a}^{p_{\text{bot}}} \frac{1}{\rho g}\, dp + \frac{(\overline{P}_a - p_a)}{\rho_s g}, \tag{A4}$$

where $p'_a = p_a - \overline{P}_a$ is the variation in surface atmospheric pressure relative to a mean $\overline{P}_a$. We approximate $\overline{P}_a$ as a constant, but actually it varies over time; in the application to satellite data, $\overline{P}_a$ is estimated as a global ocean spatial average (AVISO and PODAAC 2006). Here $H$ is the mean ocean depth at one geographic location $(\lambda, \gamma)$, $g$ is the local gravitational acceleration, $\rho_s$ is the density in the surface layer, and $\rho$ is the density in the water column. The last term in Eq. (A4) expresses the "inverted barometer" (IB) response (Doodson 1924; Wunsch and Stammer 1997) and represents the isostatic oceanic response to atmospheric pressure loads,

$$\eta_{\text{IB}} = -\frac{p_a - \overline{P}_a}{\rho_s g}. \tag{A5}$$

This surface height adjustment to $p_a$ fluctuations would by definition [Eq. (A4)] cause no change in ocean bottom pressure. This oceanic response to atmospheric pressure occurs when horizontal divergences in the water column adjust the water column height and mass to compensate for the pressure loads. This is not a compression of volume in the water column.

Wunsch and Stammer (1997), Ponte (1999), and Ponte and Gaspar (1999) discuss additional dynamical responses to atmospheric forcing under which sea level variations are not isostatic and can contribute to $p_{\text{bot}}$. The dynamic responses include barotropic modes (long gravity waves and Rossby waves) and internal modes (modified gravity waves and modified Rossby waves) (Wunsch and Stammer 1997). As we will discuss below, the PIES captures the entire spectrum of barotropic and first internal mode variability, including these dynamic (i.e., nonisostatic) responses to atmospheric forcing. Rearranging Eq. (A4) using Eq. (A5), we have

$$\eta' - \eta_{\text{IB}} + H = \int_{\overline{P}_a}^{p_{\text{bot}}} \frac{1}{\rho g}\, dp. \tag{A6}$$

Next, we show that this integral can be separated into two contributions to displacements in the free surface—$\eta_{\text{bt}}$ and $\eta_{\text{bc}}$—as follows:

$$\begin{aligned}\eta' - \eta_{\text{IB}} + H &= \int_{\overline{P}_a}^{\overline{P}} \frac{1}{\rho g}\, dp + \int_{\overline{P}}^{p_{\text{bot}}} \frac{1}{\rho g}\, dp, \\ &= \frac{1}{g}\int_{\overline{P}_a}^{\overline{P}} [\alpha(35, 0, p) + \delta]\, dp + \frac{(p_{\text{bot}} - \overline{P})}{\rho_b g},\end{aligned} \tag{A7}$$

where the local gravitational acceleration approximation near the surface $g = g(\lambda, 0)$ accounts for the dependence on latitude and neglects the vertical variation of $O(100)$ ppm in typical ocean depths. Equation (A2) defines pressure $\overline{P}$, and $\rho_b$ is the density in the bottom layer, $\alpha$ is the specific volume, and $\delta$ is the specific volume anomaly, given by

$$\delta = \alpha(S, T, p) - \alpha(35, 0, p).$$

The first integral on the right-hand side of Eq. (A7) can be expressed as the sum of the mean standard ocean depth $H_{\text{so}}$ plus sea level change caused by geopotential anomaly $\phi_{\overline{P}}$, which is calculated relative to $\overline{P}$, treating mean atmospheric pressure as zero, which is standard practice,

$$H_{\text{so}} = \frac{1}{g}\int_{\overline{P}_a=0}^{\overline{P}} \alpha(35, 0, p)\, dp \quad \text{and} \quad \frac{\phi_{\overline{P}}}{g} = \frac{1}{g}\int_0^{\overline{P}} \delta\, dp.$$

Consequently,

$$\eta' - \eta_{\text{IB}} + (H - H_{\text{so}}) = \frac{\phi_{\overline{P}}}{g} + \frac{p_{\text{bot}} - \overline{P}}{\rho_b g}. \tag{A8}$$

The first term on the right-hand side of Eq. (A8) varies because of steric or density-related changes in sea level.

In addition, when mass per square meter of water column height changes, there is a change in bottom pressure. The second term on the right-hand side of Eq. (A8) is an independent, nonsteric, part of SSH because of variable mass loading, which is equal to the time-varying barotropic component of SSH, $\eta'_{\text{bt}}$, where we remove the mean, $\eta'_{\text{bt}} = \eta_{\text{bt}} - \overline{\eta}_{\text{bt}}$. Thus,

$$\eta_{\rm bc} = \frac{\phi_{\overline{P}}}{g} \quad \text{and} \tag{A9}$$

$$\eta'_{\rm bt} = \frac{p_{\rm bot} - \overline{P}}{\rho_b g}, \tag{A10}$$

where subscripts bc and bt indicate baroclinic and barotropic, respectively.

Several previous studies have discussed SSH (after IB correction) as the sum of steric and nonsteric components resulting from the hydrostatic relationship (see, e.g., Teague et al. 1995; Ponte 1999; Jayne et al. 2003). Here, we apply the hydrostatic equation in pressure coordinates, which offers the advantage of expressing the two separate components $\eta_{\rm bc}$ and $\eta'_{\rm bt}$ in the manner in which they are measured with the PIES instruments.

*b. Converting PIES data into SSH variability*

We convert the PIES $p_{\rm bot}$ and $\tau_{\rm hourly}$ to $\eta'_{\rm bt}$ and $\eta_{\rm bc}$. The time varying term $\eta'_{\rm bt}$ in Eq. (A10) is determined directly from $p_{\rm bot}$, hourly measurements of bottom pressure from the PIES instrument. Removing the mean pressure as in Eq. (A2), $p' = p_{\rm bot} - \overline{P}$. Then,

$$\eta'_{\rm bt} = \frac{p'}{\rho_b g}. \tag{A11}$$

The value $\overline{P}$ consists of a ''leveling constant'' (Baker-Yeboah 2008) because of site-to-site differences in deployment depth plus those site-to-site differences due to the time-mean deep geostrophic velocity field. We reference all the ASTTEX pressure records to the 4500-dbar level and use $\rho_b = 1048.1$ kg m$^{-3}$ (based on ASTTEX CTD data relative to the 4500-dbar level) for each leveled PIES record. This approximation for $\rho_b$ introduces a compressibility-scale-factor error in $\eta'_{\rm bt}$ of at most $1.005 \approx 1$, which is negligible. Further details can be found in Baker-Yeboah (2008).

Next, we compute $\eta_{\rm bc}$. Previous studies (He et al. 1998; Hendry et al. 2002; Teague et al. 1995) have used Eq. (A9) to convert PIES data to $\eta_{\rm bc}$. In comparison with these works, we have augmented the PIES processing, such that we remove the small contribution to $\tau_{\rm hourly}$ from pathlength variations ($2p'/\rho_b g c_b < 0.0003$ s) associated with $\eta'_{\rm bt}$, which occur throughout the frequency spectrum. The acoustic travel time that varies purely from internal changes in the water column is given by

$$\tau_{\rm bc} = \tau_{\rm hourly} - \frac{2p'}{\rho_b g c_b}, \tag{A12}$$

where $c_b$ is speed of sound in the bottom layer and $\rho_b$ and $c_b$ are calculated from temperature, pressure, and salinity data collected during the ASTTEX deployment and recovery cruises.

The $\tau_{\rm bc}$ measurements in Eq. (A12) were used to determine the time series term $\eta_{\rm bc}$ via a procedure in which geopotential anomaly $\phi(\tau)$ is determined from a lookup curve determined from regional hydrographic data. For any deep pressure level at or below 4500 dbar, we treat the contribution to $\phi$ as a constant, $\phi_{\overline{P}} - \phi_{4500} \simeq$ constant: independent of time and uncorrelated with $\tau$ (Baker-Yeboah 2008). Under this assumption, Eq. (A9) takes the form

$$\eta_{\rm bc} = \frac{\phi_{4500}}{g} + \text{constant}, \tag{A13}$$

and we reference all the ASTTEX IES measurements to this 4500-dbar reference level (to account for differences in site-to-site deployment depths, as in the case of pressure measurements). The depths of the instruments ranged from 4501 to 5260 dbar at sites 3–12, and the depth was 1077 dbar at site 1 and 3954 dbar at site 2. For site 2, we assume that the variability at 3954 dbar is the same as that at 4500 dbar; however, site 1 is a special case (Baker-Yeboah 2008).

We use a spline-curve fitting procedure to look up geopotential anomaly as a function of acoustic travel time, similar to the procedures of He et al. (1998). In particular, the acoustic travel time index values were calculated as $\tau^*_{4500}$, where

$$\tau^*_{4500} = \frac{1}{g_o}\int_0^{4500} \frac{2}{\rho c}\, dp,$$

in which a constant value $g_o = 9.80$ m s$^{-2}$ is used, as in Watts et al. (2001), to avoid the spatial dependence of $g$ and to allow us to combine CTD measurements from different latitudes. The resulting IES lookup curve $\phi_{4500}$ versus the index $\tau^*_{4500}$ is plotted in Fig. 9. The locations are shown as black dots in Fig. 1 of the historical CTD data that were used to calculate $\phi_{4500}$ and $\tau^*_{4500}$ used to produce this lookup curve. Although additional CTD data (gray dots) were available, these did not typify the water properties in the vicinity of the ASTTEX array and therefore were not used.

At pressure levels deeper than the $p = 4500$ dbar, the velocity profile is nearly independent of depth; therefore, $p'$ at 4500 m is nearly identical to $p'$ at the bottom, where it is measured by the PIES. Analysis of $\phi_{4500} - \phi_{\overline{P}}$ from historical CTD data confirms this assumption, as the linear slope goes to zero for pressures deeper than 4500 dbar (Baker-Yeboah 2008).

The $\tau_{\rm bc}$ time series measured by the PIES instrument [Eq. (A12)] must be converted to the index $\tau^*_{4500}$, which

allows us to consistently relate $\tau$ measurements among sites at different depths. This is done using the following two relations:

$$\tau^*_{\rm bc} = \frac{g}{g_o}\tau_{\rm bc} \quad \text{and} \quad \tau^*_{4500} = A\tau^*_{\rm bc} + B, \qquad \text{(A14)}$$

where $g$ is the local value of gravity at a PIES site as a function of latitude and bottom depth (Baker-Yeboah 2008). The coefficients $A$ and $B$ are empirically determined for each PIES site from coinciding CTDs, as detailed in Baker-Yeboah (2008).

After this calibration [Eq. (A14)], the $\tau^*_{4500}$ time series at each PIES site can be used as an index to find the time series of $\phi_{4500}$ in the lookup curve in Fig. 9 and thereby determine $\eta_{\rm bc}$ from Eq. (A13). The time series $\eta_{\rm bc}$ can be separated into time-mean and variable parts $\eta_{\rm bc} = \overline{\eta}_{\rm bc} + \eta'_{\rm bc}$, where

$$\eta'_{\rm bc} = \frac{\phi'_{4500}}{g}. \qquad \text{(A15)}$$

Flowcharts and supplemental figures detailing the processing steps used are presented in Baker-Yeboah (2008).

From this point forward, we focus on the temporal variability in SSH and use the term SSH variability to refer to the time-varying contribution to SSH after the removal of the time mean relative to the period of observation. Rewriting Eq. (A8) using Eqs. (A9) and (A10) gives

$$\eta' - \eta_{\rm IB} + (H - H_{\rm so}) - (\overline{\eta}_{\rm bt} + \overline{\eta}_{\rm bc}) = \eta'_{\rm bt} + \eta'_{\rm bc}. \qquad \text{(A16)}$$

The constant terms $(H - H_{\rm so})$ and $(\overline{\eta}_{\rm bt} + \overline{\eta}_{\rm bc})$ cancel out of the equation, and thus we are left with

$$\eta' - \eta_{\rm IB} = \eta'_{\rm bt} + \eta'_{\rm bc}, \qquad \text{(A17)}$$

which expresses SSH variability, after the IB correction, as the sum of barotropic and baroclinic variability, where $\eta'_{\rm bt}$ was determined using Eq. (A11) and $\eta'_{\rm bc}$ was determined using Eqs. (A12)–(A15) along with the lookup curve in Fig. 9. For the sake of simplicity, we can rewrite Eq. (A17) in terms of total variability measured by a PIES, $\eta'_{\rm PIES}$ as

$$\eta'_{\rm PIES} = \eta' - \eta_{\rm IB} = \eta'_{\rm bt} + \eta'_{\rm bc}. \qquad \text{(A18)}$$

## REFERENCES


AVISO, 2006: SSALTO/DUACS user handbook: (M)SLA and (M)ADT near-real time and delayed time products. AVISO Rep. CLS-DOS-NT-06.034, SALP-MU-P-EA-21065-CLS, 39 pp.

—— and PODACC, 2006: AVISO and PODAAC user handbook: IGDR and GDR Jason products. AVISO Rep. SMM-MU-M5-OP-13184-CN, PODAAC Rep. JPL D-21352, 130 pp.

Baker-Yeboah, S., 2008: Sea surface height variability and the structure of eddies in the South Atlantic Cape Basin. Ph.D. dissertation, University of Rhode Island, Narragansett, 308 pp.

Biastoch, A., C. W. Boning, and J. R. E. Lutjeharms, 2008: Agulhas leakage dynamics affects decadal variability in Atlantic overturning circulation. *Nature,* **456,** 489–492.

Byrne, D. A., 2000: From the Agulhas to the South Atlantic: Measuring inter-ocean fluxes. Ph.D. dissertation, Columbia University, 162 pp.

——, and J. L. McClean, 2008: Sea level anomaly signals in the Agulhas Current region. *Geophys. Res. Lett.,* **35,** L13601, doi:10.1029/2008GL034087.

——, D. L. Witter, D. R. Watts, N. R. Pettigrew, C. M. Duncombe Rae, and S. Baker-Yeboah, 2006: Interocean heat and salt transports from the Agulhas leakage: First results from ASTTEX. *Eos, Trans. Amer. Geophys. Union,* **87** (Ocean Sci. Meeting Suppl.), Abstract OS22C–03.

Cartwright, D. E., 2000: *Tides: A Scientific History*. Cambridge University Press, 292 pp.

Chao, Y., and L.-L. Fu, 1995: A comparison between the TOPEX/POSEIDON data and a global ocean general circulation model during 1992–1993. *J. Geophys. Res.,* **100,** 24 965–24 976.

Chaplin, G. F., and D. R. Watts, 1984: Inverted echo sounder development. *IEEE Oceans '84 Conf. Record,* Vol. 1, IEEE, 249–253.

Clement, A., and A. L. Gordon, 1995: The absolute velocity field of Agulhas eddies and the Benguela Current. *J. Geophys. Res.,* **100,** 22 591–22 601.

Doodson, A. T., 1924: Meteorological perturbations of sea-level and tides. *Mon. Not. Roy. Astron. Soc.,* **1** (Geophys. Suppl.), 124–147.

Emery, W. J., and R. E. Thomson, 2001: *Data Analysis Methods in Physical Oceanography*. Elsevier, 638 pp.

Fofonoff, N., 1962: Dynamics of ocean currents. *The Sea,* M. N. Hill, Ed., Ocean Engineering Science, Vol. 1, John Wiley and Sons, 323–395.

Fukumori, I., R. Raghunath, and L.-L. Fu, 1998: Nature of global large-scale sea level variability in relation of atmospheric forcing: A modeling study. *J. Geophys. Res.,* **103,** 5493–5512.

Garzoli, S. L., and A. Gordon, 1996: Origins and variability of the Benguela Current. *J. Geophys. Res.,* **101,** 897–906.

Gille, S., and C. W. Hughes, 2001: Aliasing of high-frequency variability by altimetry: Evaluation from bottom pressure recorders. *Geophys. Res. Lett.,* **28,** 1755–1758.

Gordon, A. L., 1985: Indian-Atlantic Transfer of Thermocline Water at the Agulhas Retroflection. *Science,* **227,** 1030–1033.

Guinehut, S., P.-Y. LeTraon, and G. Larnicol, 2006: What can we learn from global altimetry/hydrography comparisons? *Geophys. Res. Lett.,* **33,** L10604, doi:10.1029/2005GL025551.

He, Y., D. R. Watts, and K. L. Tracey, 1998: Determining geostrophic velocity shear profiles with inverted echo sounders. *J. Geophys. Res.,* **103,** 5607–5622.

Hendry, R. M., D. R. Watts, and C. S. Meinen, 2002: Newfoundland Basin sea-level variability from TOPEX/POSEIDON altimetry and inverted echo sounder-bottom pressure measurements. *Can. J. Remote Sens.,* **28,** 544–555.

Houston, M. H., and J. M. Paros, cited 1998: High accuracy pressure instrumentation for underwater applications. *Proc. Int. Symp. on Underwater Technology,* Tokyo, Japan, IEEE, 307–311, doi:10.1109/UT.1998.670113. [Available online at http://www.paroscientific.com/uwapp.htm.]

IESUM, cited 2006: Inverted echo sounder user's manual. [Available online at http://po.gso.uri.edu/dynamics/IES/index.html.]

Jayne, S. R., J. M. Wahr, and F. O. Bryan, 2003: Observing ocean heat content using satellite gravity and altimetry. *Geophys. Res. Lett.,* **108,** 3031, doi:10.1029/2002JC001619.

Luther, D. S., A. D. Chave, J. H. Filloux, and P. F. Spain, 1990: Evidence for local and nonlocal barotropic responses to atmospheric forcing during BEMPEX. *Geophys. Res. Lett.,* **17,** 949–952.

Munk, W. H., and D. E. Cartwright, 1966: Tidal spectroscopy and prediction. *Philos. Trans. Roy. Soc. London,* **A259,** 533–581.

Olson, D. B., R. A. Fine, and A. L. Gordon, 1992: Convective modifications of water masses in the Agulhas. *Deep-Sea Res.,* **39,** S163–S181.

Ponte, R. M., 1999: A preliminary model study of the large-scale seasonal cycle in bottom pressure over the global ocean. *J. Geophys. Res.,* **104,** 1289–1300.

——, and P. Gaspar, 1999: Regional analysis of the inverted barometer effect over the global ocean using TOPEX/POSEIDON data and model results. *J. Geophys. Res.,* **104,** 15 587–15 601.

Schwiderski, E. W., 1982: Global ocean tides. Part X: The fortnightly lunar tide (MF) atlas of tidal charts and maps. Naval Surface Weapons Center Tech. Rep. 820151, 87 pp.

Stammer, D., C. Wunsch, and R. M. Ponte, 2000: De-aliasing of global high frequency barotropic motions in altimeter observations. *Geophys. Res. Lett.,* **27,** 1175–1178.

Sun, C., and D. R. Watts, 2001: A circumpolar gravest empirical mode for the Southern Ocean hydrography. *J. Geophys. Res.,* **106,** 2833–2855.

Teague, W. J., Z. R. Hallock, G. A. Jacobs, and J. L. Mitchell, 1995: Kuroshio sea surface height fluctuations observed simultaneously with inverted echo sounders and TOPEX/POSEIDON. *J. Geophys. Res.,* **100,** 24 987–24 994.

Tierney, C., J. Wahr, F. Bryan, and V. Zlotnicki, 2000: Short-period oceanic circulation: Implications for satellite altimetry. *Geophys. Res. Lett.,* **27,** 1255–1258.

Van Aken, H. M., A. K. Van Veldhoven, C. Veth, W. De Ruijter, P. Van Leeuwen, S. Drijfhout, C. P. Whittle, and M. Rouault, 2003: Observations of a young Agulhas ring, Astrid, during MARE in March 2000. *Deep-Sea Res. II,* **50,** 167–195.

Watts, D. R., and H. T. Rossby, 1977: Measuring dynamic heights with inverted echo sounders: Results from MODE. *J. Phys. Oceanogr.,* **7,** 345–358.

——, and H. Kontoyiannis, 1990: Deep-ocean pressure measurement: Drift removal and performance. *J. Atmos. Oceanic Technol.,* **7,** 296–306.

——, C. Sun, and S. Rintoul, 2001: A two-dimensional gravest empirical mode determined from hydrographic observations in the subantarctic front. *J. Phys. Oceanogr.,* **31,** 2186–2209.

Wunsch, C., and D. Stammer, 1997: Atmospheric loading and the oceanic inverted barometer effect. *Rev. Geophys.,* **35,** 79–107.

Xu, Y., J.-H. Park, and D. R. Watts, 2008: De-aliasing of large-scale high-frequency barotropic signals from satellite altimetry in the Japan/East Sea. *J. Atmos. Oceanic Technol.,* **25,** 1703–1709.